





Microbubble Contrast Agents Improve Detection of Active Hemorrhage

Scott Schoen Jr , Member, IEEE, Alexis Prasov, Ion Candel, Saaid Arshad, Mark Ottensmeyer , Theodore T. Pierce , Laura J. Brattain, Senior Member, IEEE, Brian A. Telfer , Senior Member, IEEE, and Anthony E. Samir

Abstract—Assessment of trauma-induced hemorrhage with ultrasound is particularly challenging outside of the clinic, where its detection is crucial. The current clinical standard for hematoma detection – the focused assessment with sonography of trauma (FAST) exam – does not aim to detect ongoing blood loss, and thus is unable to detect injuries of increasing severity. To enhance detection of active bleeding, we propose the use of ultrasound contrast agents (UCAs), together with a novel flow phantom and contrast-sensitive processing techniques, to facilitate efficient, practical characterization of internal bleeding. Within a the custom phantom, UCAs and processing techniques enabled a significant enhancement of the hemorrhage visualization (mean increase in generalized contrast-to-noise ratio of 17%) compared to the contrast-free case over a range of flow rates up to 40 ml/min. Moreover, we have shown that the use of UCAs improves the probability of detection: the area under the receiver operating characteristic curve for a flow rate of 40 ml/min was 0.99, compared to 0.72 without contrast. We also demonstrate how additional processing of the spatial and temporal information further localizes the bleeding site. UCAs also enhanced Doppler signals over the non-contrast case. These results show that specialized nonlinear processing (NLP) pipelines together with UCAs may offer an efficient means to improve substantially the detection of slower hemorrhages and increase survival rates for trauma-induced injury in pre-hospital settings.

Index Terms—Trauma, hemorrhage, contrast agents, ultrasound, doppler.

Impact Statement—We show in vitro that ultrasound contrast agents and tailored post-processing techniques to visualize them can enhance detection and characterization

Manuscript received 18 January 2024; revised 19 April 2024 and 12 June 2024; accepted 12 June 2024. Date of publication 18 June 2024; date of current version 7 November 2024. This work was supported by the Department of the Army under Air Force under Contract FA8702-15-D-0001 (Combat Casualty Care Research Program). The review of this article was arranged by Editor Riccardo Barbieri. (*Corresponding author: Scott Schoen Jr.*)

Scott Schoen Jr, Ion Candel, Mark Ottensmeyer, Theodore T. Pierce, and Anthony E. Samir are with the Center for Ultrasound Research and Translation, Harvard Medical School and Massachusetts General Hospital, Boston, MA 02114 USA (e-mail: sschoenjr@mgh.harvard.edu).

Alexis Prasov, Saaid Arshad, and Brian A. Telfer are with the MIT Lincoln Laboratory, Lexington, MA 02421 USA.

Laura J. Brattain is with the University of Central Florida, Orlando, FL 32816 USA.

This article has supplementary downloadable material available at <https://doi.org/10.1109/OJEMB.2024.3414974>, provided by the authors.

Digital Object Identifier 10.1109/OJEMB.2024.3414974

of active hemorrhage, a leading cause of trauma-related deaths world-wide.

I. INTRODUCTION

PHYSICAL trauma (i.e., tissue injury due to sudden forces, hereafter “trauma”) causes 5 to 6 million deaths every year worldwide [1] and is among the leading causes of death among those less than 50 years of age [2]. In trauma, induced hemorrhaging (most commonly to solid organs such as liver, kidney, and spleen [3]) is the leading cause of morbidity after central nervous system injury [4], [5]. Hemorrhage is also the leading cause of preventable death among combat and civilian trauma casualties [6], [7], with torso hemorrhage in particular responsible for 60% of potentially preventable deaths on the battlefield. Most potentially preventable deaths due to hemorrhage occur early after injury [5], which motivates the need for technologies to better control bleeding [8], [9] and to perform damage-control resuscitation in pre-hospital settings or emergency departments [10]. Unfortunately, it is in such locations, where advanced image guidance would facilitate prompt treatment, that imaging resources are often more limited [11].

Ultrasound (US) has several advantages over other modalities for hemorrhage detection such as multidetector CT angiography [12], [13]: not only is it much more portable, but also it is significantly cheaper and requires no ionizing radiation. The clinical standard for identifying patients at risk of life-threatening traumatic hemorrhage is the focused assessment with sonography in trauma (FAST) exam [14]. The FAST exam comprises examination of standard US views (right/left upper quadrant, pelvic, pericardial, and anterior thoracic) for the presence of anechoic fluid collection, indicating extravasation of blood from the vasculature. The FAST exam has demonstrated very high specificity for the presence of free fluid: studies have reported a FAST exam sensitivity of 80% to 88% and specificity of 98% to 100% for adults [15]. For certain conditions however, lower sensitivity is reported as a key limitation of FAST: sensitivities for torso hemorrhage have been reported as low as 51% in Level 1 trauma centers [15], and sensitivities / specificities of 75% / 99% [16] and 56% / 98% [17] in Role 2 care, respectively. Crucially, the FAST exam is limited in that it is unable to distinguish active bleeding and cannot localize the source of a hemorrhage (beyond identifying a torso quadrant). Thus, there

is an opportunity to leverage newer ultrasound techniques to enhance assessment of active hemorrhage.

Over the last several decades, the development and deployment of commercial US contrast agents (UCAs, i.e., microbubbles with radii $R \sim 2 \mu\text{m}$ which comprise encapsulated gas cores surrounded by a stabilizing shells) has facilitated the rapid proliferation of contrast-enhanced US (CEUS) techniques [18], [19]. CEUS offers several potential enhancements to the FAST exam, namely 1) increased sensitivity, 2) the ability to detect ongoing bleeding, and 3) the potential to locate the source of bleeding. CEUS is currently used for other indications, particularly examinations of the heart and liver. These agents are attractive for hemorrhage detection in that they are safe and well-tolerated [20], [21], readily available, and have half-lives on the order of a few minutes after administration [22], [23]. They are significantly safer than CT contrast agents, as UCAs are not nephrotoxic and the incidence of life-threatening allergic reaction is orders of magnitude lower [24]. UCAs are also safe to use in patients with poor kidney function or acute kidney injuries, unlike MRI contrast agents [25].

With respect to sensitivity, CEUS has been compared to conventional FAST for detecting free abdominal fluid; a recent survey of ten studies with 1359 human patients found a sensitivity / specificity of 93%/99% compared to 56%/98% for FAST [26]. Other applications of CEUS for trauma were surveyed in Eisenbrey et al. [27]. UCAs are also attractive due to their potential to distinguishing between active bleeding and bleeding that has stopped, which may occur due to the body's compensatory measures [28]. MRI or CT contrast agents may diffuse into the interstitial space from healthy vessels [29], and the FAST exam will detect free abdominal blood, even if the bleeding has stopped. UCAs, on the other hand, will only be present outside of the vasculature if there is active bleeding when the contrast agent is introduced.

Of particular interest in this work is the suite of image- and signal processing tools developed in the last 10 years that seek to isolate microbubble-specific signals and enable super-resolution (i.e., below the classical diffraction limit) ultrasound imaging of the microvasculature [30]. These are particularly attractive as they are post-processing methods that are agnostic to the nature of the US acquisition itself, but face challenges in translation due to the higher frequencies and frame rates required (compared to typical clinical diagnostic US) and to the required spatiotemporal separation of the signals which is difficult to control *in vivo* [31], [32]. However, in the case of hemorrhage localization, microscale resolution is not essential since these injuries and flow velocities occur at the centimeter scale. Thus while CEUS has already shown promise toward the detection of the existence of blood pools [33], [34], the ability of novel processing may yet enable elucidation of injury hemodynamics, and therefore enhance US's diagnostic capability for traumatic injuries.

The potential of localizing the bleeding source with CEUS has not been quantified before, although this potential has been suggested [26], [27]. Noninvasively localizing the bleeding source with an ultrasound system that is more portable than CT would be a valuable capability in pre-hospital care, such as for damage control surgery in an austere setting. The objective of the work

reported herein is to quantify the minimum flow hemorrhage that can be detected in a hemorrhage phantom, analogous to research conducted to quantify minimum detectable hemorrhage rates for multi-detector computed tomography (MDCT) compared to digital subtraction angiography [35], which identified an empirical threshold of 0.35 mL/min to identify bleeding from sub-millimeter diameter vessels.

To this end, we describe the development of an *in vitro* test platform to mimic an abdominal hemorrhage, as well as a non-linear processing (NLP) pipeline, and demonstrate the pipeline's ability to enhance US signals related to active bleeding. We then characterize the improvement via the pipeline both with and without UCAs at clinical concentrations, at a range of bleeding rates and compared to Doppler. Finally, we quantify the degree of enhancement of the processed images towards assessing the ability of a sonographer to identify hemorrhage signals from them in support of clinical decision-making.

II. METHODS AND MATERIALS

A. Flow Phantom

To simulate an abdominal hemorrhage, we designed and fabricated a custom flow phantom, comprising a centimeter-scale vessel, millimeter-scale vessel perforation, and a narrow hematoma-mimicking fluid cavity. The design reflected a balance of anatomical fidelity with reliable fabrication and repeatable experimental setup. Hollow, water-soluble vessel-and-cavity geometry was 3D printed in butenediol vinyl alcohol copolymer (1.75 mm BVOH filament, Verbatim GmbH, Germany) and then brush-coated with two layers of 20 Shore A platinum-cure silicone (Dragon Skin 20, Smooth-On, Inc., Macungie, PA, USA, Young's modulus approximately 850 kPa, density 1080 kg/mm³). The printed structure was suspended in an external mold that was then filled with tissue-mimicking gel (water with 3% (w/w) agar and 1% (w/w) cellulose to provide distributed scattering). Finally, water was flowed through the vessels to dissolve the printed material leaving a hollow, vessel-mimicking silicone lumen embedded in the echogenic gel.

B. Data Collection

The experimental setup is illustrated in Fig. 1 and described briefly here. Lumason contrast agents (Bracco, Monroe Township, NJ, USA) were prepared according to manufacturer instructions and combined with a conventional blood-mimicking fluid [36], [37] [specifically, water with cornstarch, 1% (w/w) to simulate red blood cell scattering] at the clinical concentration assuming uniform distribution (equivalent to 0.04 ml/kg for a 70 kg adult, resulting in a concentration 7.2 to 27 $\times 10^4$ UCAs per milliliter of blood simulant). The UCAs and simulant were drawn through the hemorrhage at controlled rates between 0 ml/min and 40 ml/min via a programmable syringe pump (KD Scientific, Holliston, MA, USA). The UCAs and fluid were kept in a beaker reservoir with a stir blade at 150 revolutions per minute to maintain distribution.

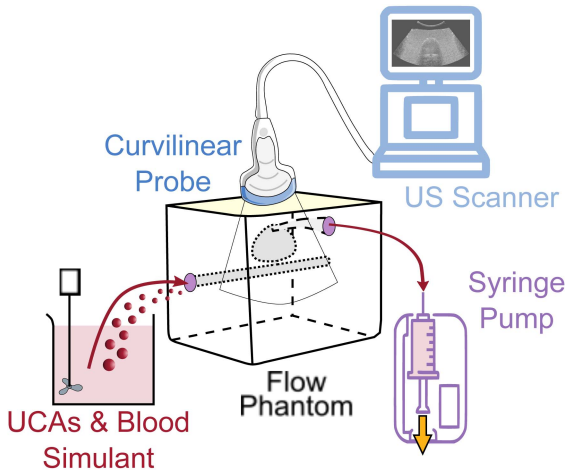


Fig. 1. Experimental setup: Contrast agents are kept in suspension of a blood simulant, and drawn at a controlled rate through the hemorrhage phantom via a programmable syringe pump. Images are captured on a commercial US scanner and the cine-loops stored for offline processing.

Ultrasound images were collected with GE LOGIQ E10 (GE Healthcare, Chicago, IL USA), with a C1-6VN curvilinear probe (192 elements, ROC 55 mm, center frequency 3.5 MHz) positioned on a mechanical arm that was stationary for all acquisitions. Steady-state flow of the bubble/simulant mixture was established, and then each dataset was acquired. Cine-loops comprising 112 to 263 frames (1.7 to 4.0 s) were acquired at 4.5 MHz with default abdominal “detail” settings to a depth of 9 cm to encompass a field of view containing the simulated vessel lumen and hematoma. The probe was placed on an acoustically transparent standoff pad (Parker Laboratories, Fairfield, NJ, USA) to protect the phantom surface, and manually aligned at a shallow angle to ensure the bleed and lower portion of the hematoma were visible. For Doppler images, the Doppler sensitivity was adjusted manually, and such that there was no appreciable Doppler signal at the zero flow condition (± 18 cm/s); this setting was retained for all acquisitions.

C. Nonlinear Processing

The collected image stacks were processed according to a series of contrast-selective processing techniques initially proposed for the ultrasound localization microscopy to identify distributed contrast agents. All processing schemes were implemented in MATLAB (R2022a/R2022b, The Mathworks, Natick, MA USA) and run on a general purpose workstation (Intel Core i9-10900, 32 GB memory). The processing flow, which may be used with arbitrary transmit/receive schemes that renders grayscale image sequences, is illustrated in Fig. 2.

1) SVD Filtering: To suppress signals due to static structures (e.g., tissue), the image stack was processed with a singular value decomposition filter [38]. Briefly, the individual frames are reshaped to a $N_x N_z \times N_t$ matrix, whose singular values and vectors are found. The ordered singular vectors u_i corresponding to slowly-changing, spatially correlated image features have the largest singular values σ_i , while those with the smallest singular values do not correspond to meaningful signals; the

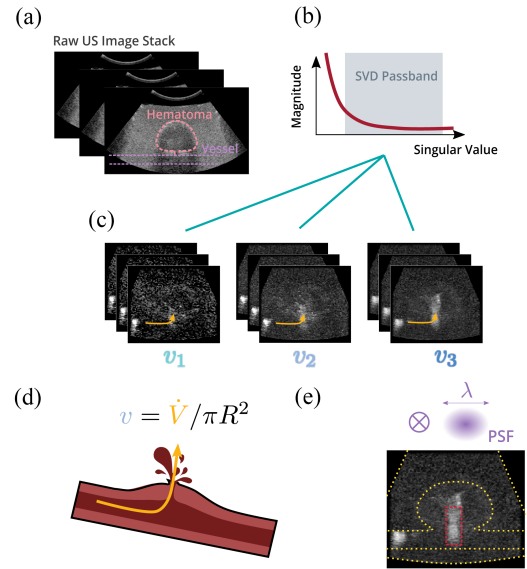


Fig. 2. Processing pipeline. (a) Raw ultrasound image stacks are captured as depicted in Fig. 1. (b) SVD processing is performed to reject static (tissue) signal and noise. (c) Microbubble separation is performed to isolate signals that move within a certain range of speeds. (d) The expected exit velocity is computed based on the target flow rate. (e) The separated images at the target flow rate are deconvolved with a point spread function with an estimated PSF (purple). For evaluation, the bleed signal (red) and noise (yellow) regions are defined.

SVD filter thus sets the weights for the first few and last several vectors to 0, and re-assembles the image stack [38]. The optimal set of singular values to exclude depends on the nature of the dataset (specifically the rate of the motion of interest and the duration and frame rate of the sequence [39]), and thus is usually set empirically. In this work, to account for the varying flow rates and image durations acquired, we chose empirically to retain singular values greater than 4 and less than 100 for all image sets.

2) UCA Separation: Following SVD filtering, the data were further filtered with a microbubble separation algorithm proposed by Huang et al. [40]. This technique enables spatiotemporal filtering of the image sequence to enhance only signals that move at rates within a specified range of velocities—including both magnitude and direction. Briefly, if the intensity distribution due a UCA at position \mathbf{r} is $s(\mathbf{r})$, then its signal over time is given by $s(\mathbf{r} - \mathbf{v}t)$, where \mathbf{v} is the UCA’s velocity. Thus if we consider a Fourier transform of the image stack, then signals that move with velocities in some range $[v_1, v_2]$ are associated with particular spatial frequencies $\|k\| \in [\omega/\|v_1\|, \omega/\|v_2\|]$. Importantly, this filtering is completed entirely in post-processing and does not impose any particular requirements on the data collection itself, except that spatial and temporal sampling of the frames must be sufficient to support the velocities and spatial scales of interest.

Image stack acquisitions were filtered at velocity ranges $v_z \in v_{\text{exit}}[0.5, 2.0]$, where v_{exit} is the expected exit velocity for the size r_0 of the perforation $v_{\text{exit}} = \dot{V}/\pi r_0^2$, and \dot{V} is the volume flow rate. While this range was selected based on the estimated exit velocity (which would not be known *a priori*

for *in vivo* acquisitions), this post-processing parameter may be set to identify signals associated with any velocity ranges after acquisition. The filter was made directional by requiring that $\omega k_z \geq 0$, where k_z is the vertical wavenumber component. Finally, to reduce Gibbs effects that might be introduced by the binary threshold cutoff, the 3D binary mask was blurred with an 8 voxel Gaussian kernel to achieve smoother windowing in the frequency domain.

3) Deconvolution: Finally, the separated frames were individually passed through an iterative deconvolution [41], [42] filter to further enhance microbubble signals. The deconvolution served to reduce the effect of diffraction in the imaging process due to the point scatterers the UCAs represent. Approximating the point spread function of the imaging as a Gaussian distribution of wavelength order enabled better isolation of UCA-specific signals. A kernel of two wavelengths (0.7 mm) in each dimension was deconvolved with each frame for four iterations.

D. Evaluation

1) Image Metrics: To assess the performance of UCAs to enhance the detection of bleeding compared to the contrast-free case, as well as any improvement given by the processing pipeline, we computed the generalized contrast to noise ratio (gCNR), the probability of detection, and the probability of false alarm. All metrics were evaluated on the image stack (i.e., the composite image formed by the summation of all frames over a specified duration) for each case, with and without UCA, for the processed pipeline.

The gCNR aims to ameliorate bias present in other metrics (such as contrast or typical CNR) that may be affected by the dynamic range, as well as to map better to perceived detectability and trend more predictably with added noise [43]. The gCNR is computed by evaluating the cumulative distribution functions of the distributions of pixel intensities in the two regions of interest (i.e., signal and background). A gCNR of 1 indicates no overlap between the distribution of signal intensities in the signal and reference regions, while a gCNR of 0 indicates nearly equivalent distributions (and thus no contrast; see Supplementary Material). To assess the contrast changes between flow rates and with- and without UCAs, we used Welch's two-tailed *t*-test [44] to compare the distribution of gCNRs from the image stack over all acquisitions ($N = 4$ for each flow rate and UCA condition).

2) Detection Probabilities: The probability of detection (PD) and probability of false alarm (PFA) are captured in the receiver operating characteristic (ROC) curve, which maps the true positive rate and false positive rate as they vary with a given detection threshold. Here, we varied a pixel intensity threshold T ; pixels with intensities above this threshold within the bleed region were considered true positives, while pixels above this threshold outside the bleed region were false positives. In this way, each threshold value is mapped to a point on the ROC (see Supplementary Material). The area under the curve (AUC) of the ROC thus serves to quantify the likelihood of the methodology to identify bleeding: an AUC of 1 indicates perfect detection with

no false alarms, while an AUC of 0.5 indicates the detection is no better than chance.

The PD and PFA quantify the ability of our processing pipeline to correctly extract and differentiate the desired signal (i.e. UCAs) from the background signal and noise. Given that every pixel is an opportunity for a detection, our probabilities were calculated on the composite image on a per-pixel basis. Bleed and non-bleed regions are defined in Fig. 4. To standardize the threshold intensities T between images with varying raw intensity values, the threshold was normalized to the intensities of pixels within each image stack. A detection was declared for any pixel, $p \in \mathbf{p}$, that exceeded the dynamic threshold

$$T = \text{med } \mathbf{p} + k \cdot \text{std } \mathbf{p}, \quad (1)$$

where med and std are the median and standard deviation operators, respectively, \mathbf{p} is the vector of all pixel intensities in the composite image, and k is a parameter that is varied to define the operating point on the ROC curve, and typically encompassed the entire intensity range for $k = 10$. Note that the value of T was thus calculated separately for each image stack.

3) Image Masking: Finally, to enhance detection capabilities and remove spurious measurements more likely to be false, we binarized the composite image such that pixels larger than the threshold T , defined by (1) (for some value of k), were set to 1. Then, confirmed bleeding is defined by the connected regions that occupy at least 10% of the estimated bleed site area (heuristically chosen, in this case roughly 10^3 pixels). Connected regions smaller than this threshold are postulated to be background.

III. RESULTS

A. NLP and UCAs Improve Hemorrhage Detection

To determine the effect of UCAs on the ability to detect bleeding, we considered the range of per-window gCNRs observed in the signal region when UCAs were used, vs blood simulant alone. Fig. 3 shows that UCAs provided significantly higher NLP signal levels at all non-zero flow rates. Additionally, the per-experiment ($N = 4$ for each flow rate) level was significantly different for each flow rate. To illustrate the method's ability to localize the bleeding site, we compared the signal levels (as quantified by the per-window gCNR) at the bleed site to those in the rest of the hematoma; that is we compared the bleeding site to locations that were accessible to the UCAs, but where their motion was expected to be different from that selected for by NLP (e.g., lateral or downward velocity, speed far below expected ejection rate, etc.). From Fig. 4(a), we observed that the signal at the bleed site (purple ROI) was significantly higher than in the rest of the hematoma region (yellow ROI). We observed a similar effect, though at lower gCNR values, when no UCAs were used, but for which the scatter motion would be subject to the same flow dynamics; see Fig. 4(b).

B. PD and PFA Analysis

Fig. 5 captures the performance curves for all experiments with a bleed rate of 40 ml/min, 20 ml/min, 10 ml/min, and

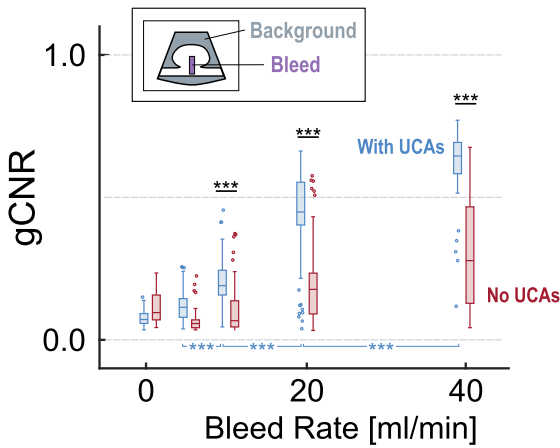


Fig. 3. UCAs & NLP Improve Contrast at Bleeding Sites. Boxes and whiskers show distribution of computed gCNRs over 10-frame intervals of the processed image stack for the bleed site (see inset). Blue distributions are from signals with UCAs and red boxes represent the no UCA case. Asterisks indicate significance levels between indicated distributions: $*$ = $p < 0.05$, $**$ = $p < 0.01$, and $***$ = $p < 0.005$. The background ROI (gray in inset) includes the entire imaging field of view outside the hematoma and vessel.

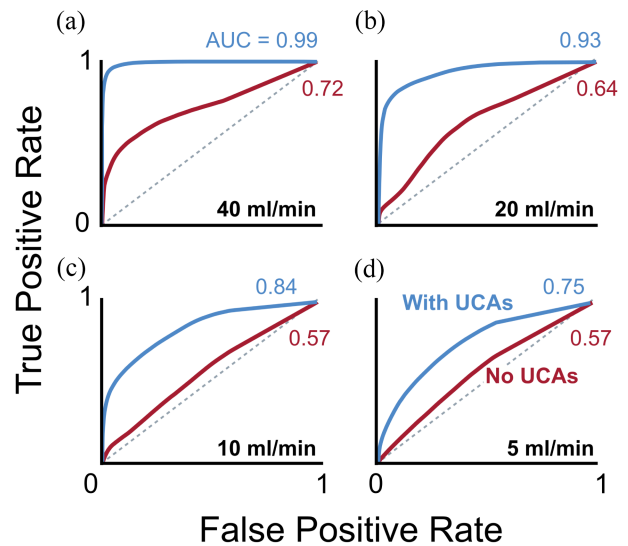


Fig. 5. Contrast Improves Detection Performance. Plots show receiver operating characteristic curves for (a) 40 ml/min, (b) 20 ml/min, (c) 10 ml/min, and (d) 5 ml/min, both with (blue) and without (red) UCAs. Also indicated are the areas under the curve, compared with the case of pure chance (dashed gray lines, AUC = 0.5).

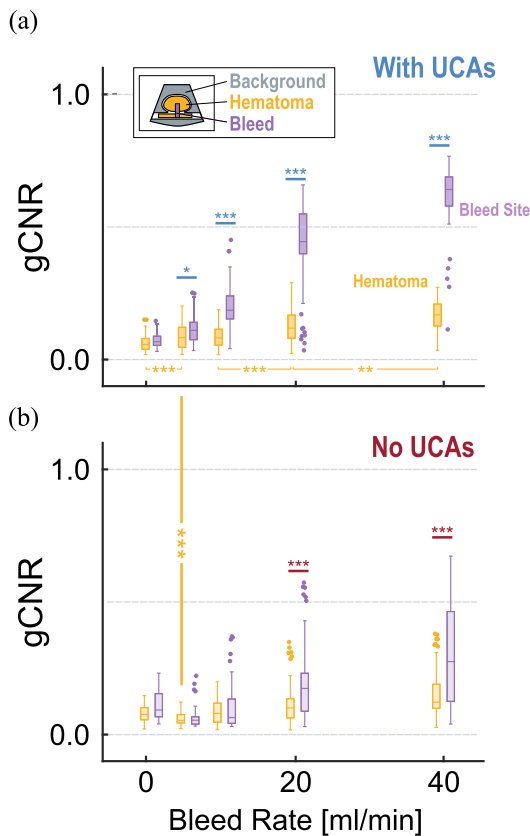


Fig. 4. NLP with UCAs Localizes Hemorrhage. (a) Signals detected in the bleed region (purple bars, same as data from Fig. 3) when UCAs were significantly higher than those in the vessel and rest of the hematoma (yellow) for all non-zero flow rates. (b) When no UCAs are present, the NLP still offered enhancement in the bleed region, but only at higher flow rates (above 20 ml/min). The difference between the contrast and non-contrast signals within the hematoma was not significant (except at 5 ml/min, vertical yellow line).

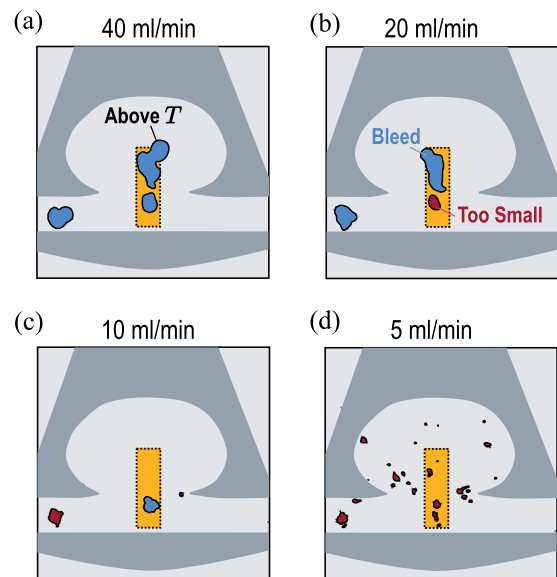


Fig. 6. Image Masking Enhances Hemorrhage Localization Performance. Background and hematoma demarcated in gray; bleeding site is in yellow. Pixels that satisfy the T criteria from (1) with $k = 3$, but fail spatial filtering in red. Pixels that satisfy the T criteria and spatial masking in blue. In these typical examples, spatial filtering localizes bleeding site for (a) 40 ml/min and (b) 20 ml/min; marginally localizes for (c) 10 ml/min, and does not detect (d) 5 ml/min rates.

5 ml/min, with and without UCAs. The use of contrast improves our ability to detect the active bleeding. For the no-flow case, 0 ml/min, there is no significant difference in the detection performance with and without contrast, producing AUCs representative of chance, i.e., 0.5. Fig. 6 shows a representative set of realizations of the image masking technique, for the operating point $k = 3$ in (1): blue regions are bleeding detections that are

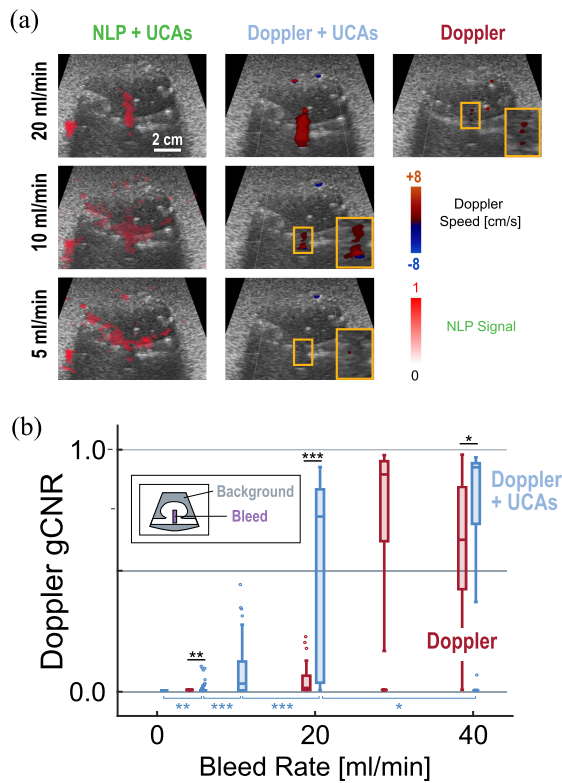


Fig. 7. (a) Representative NLP and Doppler composite frames for various flow rates. Top row shows NLP, Doppler with UCAs [blue bars in (b)], and Doppler without UCAs (red bars). (b) Distributions of time-batched (250 ms) Doppler frames with (blue) and without (red) UCAs. A settings error recorded default Doppler signals at 30 ml/min instead of 10 ml/min. Asterisks indicate significance levels between indicated distributions: $* = p < 0.05$, $** = p < 0.01$, and $*** = p < 0.005$.

sufficiently large, while red regions are rejected. This masking is able to discern the bleeding site at flows of about 10 ml/min or more, with few or no false positives (i.e., signal outside the bleed region). Connected regions of pixels within the vessel are retained in some cases, as in Fig. 6(a) and (b), as expected. Overall, this image masking with UCAs improves upon the performance curves shown in Fig. 5 and reinforces that CEUS with NLP improves hemorrhage detection.

C. CEUS Enhances Doppler

As flow is often mapped with Doppler imaging, we next evaluated the results of Doppler imaging compared with the NLP processing described above. Fig. 7(a) demonstrates the better visibility of the total NLP signals compared with Doppler, especially at flow rates below 10 ml/min. While the bleeding is plainly visible in both modalities above 20 ml/min, Doppler is inherently less sensitive to motion with a small axial component. The addition of UCAs significantly boosts the Doppler signal (compare top row, second and third column). To quantify this improvement, we compared the gCNR of the Doppler signals in the bleed site compared to the background in Fig. 7(b) (as in Figs. 3 and 4). The Doppler signal was significantly higher with UCAs than without, and the UCAs enabled reliable discernment of the flow rate (i.e., higher flow rates had significantly higher

gCNRs). Thus, while the NLP + UCAs technique has several benefits compared to Doppler + UCAs (e.g., it can work with arbitrary acquisitions and is not restricted to vertical flow), the use of UCAs alone was sufficient to improve the detection and quantification of hemorrhage with Doppler.

IV. DISCUSSION

The primary objective of this investigation was to quantify a minimum hemorrhage flow rate that can be detected and localized with contrast-enhanced ultrasound and NLP techniques. To support that objective, we designed and fabricated a hemorrhage-mimicking ultrasound phantom. We found that simulated hemorrhage with flow rates as low as 10 ml/min can be detected, with UCAs and NLP, followed by temporal integration. Detection improves with higher flow rates (tested up to 40 ml/min), as expected. While a threshold of 40 ml/min is an order of magnitude higher than that measured by others for contrast-enhanced CT, a hemorrhage of 10 ml/min will require 100 min to reach a liter of blood loss, a threshold for hemorrhagic shock. This time allows the potential for life-saving interventions in a pre-hospital setting, such as austere damage control surgery roles of care.

We find that UCAs significantly enhance signals related to bleeding, both via the NLP pipeline (Figs. 3 and 5) and via Doppler acquisitions (Fig. 7) at flow rates below 10 ml/min. Additionally, the NLP technique demonstrated high sensitivity, low false alarms (Fig. 5), and when coupled with subsequent masking, exhibited suppression of signals that were likely noise (Fig. 6). While the Doppler and NLP had similar sensitivities when UCAs were used, the latter approach has several advantages compared to Doppler: (1) The NLP technique is not restricted to measuring the axial velocity component as Doppler is. Indeed the probe position in this study gave best-case Doppler results, as the velocity was largely vertical and aligned with the probe; (2) The NLP comprises only post-processing, and does not require a Doppler acquisition (or place any restrictions on the nature of the acquisitions); further, it may filter for flow rates retrospectively, whereas Doppler requires the velocity sensitivity to be set at acquisition; (3) NLP enables potential application of localization and tracking techniques [30], [45], [46] (see Supplementary Material). Finally, while the processing in this study was performed offline, its relative efficiency (approximately 150 ms per frame without optimizations, which could be reduced significantly by removing the need to re-load the images and pre-computing the separation filters) suggests its real-time implementation is feasible.

The current study has several limitations that will be addressed in future work. While providing a repeatable experimental test bed, the flow phantom has limited anatomical fidelity. First, the phantom represents only a hemorrhage condition and not an uninjured condition for comparison. Additionally, the tissue representation is uniform, whereas human anatomy includes perfused organs in which UCAs will also be visible. Similar to earlier work [35], this simplified phantom presumes a sonographer knowledgeable of the healthy anatomy, and sought to assess flow rates at which they might reliably identify extravascular

flow. Finally, the simulated bleed represents one manifestation of hemorrhage, namely bleeding from a relatively large vessel, as opposed to other types of hemorrhage, such as blood oozing from the surface of a ruptured organ, bleeding from capillaries, or effects of hemorrhagic tamponade. Future work will incorporate more sophisticated phantoms (including non-injured and other vascularized organs) and *in vivo* testing (where such structures are inherent and plentiful) to better characterize performance in realistic scenarios.

The nonlinear processing was designed to enhance UCAs with a range of velocities for relevant hemorrhage rates. However, UCAs that have settled in a hematoma with near-zero velocities also indicate active bleeding and are thus important to detect; enhancing visibility of stationary UCAs will be addressed in future work—including by intentional elimination of circulating UCAs to retain only those which have extravasated, and thus indicate ongoing bleeding at the time of UCA introduction. Additionally, to achieve significant SNR in the raw images, the acoustic output (mechanical index 1.4) was above the recommended limit for Lumason (0.8), although still within human safety limits. It is conceivable that such high values may have effects on the integrity of the bubble shells, and thus reduce the contrast they provide. Finally, only a single UCA concentration (i.e., the standard clinical dose) was evaluated; future work will indicate whether different concentrations might enhance, e.g., separability for tracking [32].

Still, the results from this work indicate significant promise in the use of UCAs and the nonlinear processing pipeline. For instance, contrast-specific imaging sequences provide a means of selecting for microbubbles [47], [48], rather than simply moving, sub-wavelength scatterers (as was done for this work). This would provide significant benefit to localization based techniques, and perhaps realize the potential for more granular tracking and quantification (see Supplementary Figure S-3). Finally, the massive advances in machine learning architectures and approaches [49], including for microbubble detection [50] and specifically to address the present challenge of high density signals [51], suggest that there is ample opportunity to further enhance US's ability to detect and mitigate the threat of unchecked hemorrhage.

V. CONCLUSION

Untreated hemorrhaging contributes significantly to traumatic deaths worldwide. Here we have proposed an *in vitro* ultrasound phantom to mimic bleeding, and shown that UCAs significantly enhance the detectability of bleeding at clinically relevant rates, by both non-linear post-processing, and conventional colorflow Doppler. The availability and safety profile of UCAs suggest they may play an important role in the detection, and subsequent mitigation, of active bleeding and reduce overall mortality.

AUTHOR CONTRIBUTIONS

LB, TTP, AES, SS, and BT conceived the work and directed the research. LB, MO, TTP, SS, and BT contributed to the phantom design, and MO fabricated the flow phantom. SA and SS performed data collection. IC, AP, and SS performed

post-processing and data analysis. All authors contributed to drafting of the manuscript and have approved its contents.

CONFLICT OF INTEREST

AES has provided consulting for General Electric, Resolve Stroke, Ochre Bio, Rhino Healthtec, and Gerson Lehman Group; is a member of the advisory or scientific boards for General Electric, Rhino Healthtech, Ochre Bio, Resolve Stroke, and FNIH; has received research support from Canon, Echosens, General Electric, Philips, Siemens, and Supersonic Imagine/Hologic; has received research funding from Analogic Corporation, the US Department of Defense, Fujifilm Healthcare, FNIH, NIH, and General Electric; and owns equity in Avira, Autonomus, Evidence Based Psychology, Klea, Katharos Labs, Quantix Bio, Rhino Healthtech, Ochre Bio, and Resolve Stroke. SS discloses unrelated consulting for Iota Biosciences. All other authors declare no competing financial interests with respect to this work.

ACKNOWLEDGMENT

Any opinions, findings, conclusions, or recommendations expressed in this material are those of the authors and do not necessarily reflect the views of the Dept of the Army.

REFERENCES

- [1] N. D. Rossiter, "Trauma—the forgotten pandemic?," *Int. Orthopaedics*, vol. 46, no. 1, pp. 3–11, Jan. 2022.
- [2] R. Lozano et al., "Global and regional mortality from 235 causes of death for 20 age groups in 1990 and 2010: A systematic analysis for the Global Burden of Disease Study 2010," *Lancet*, vol. 380, no. 9859, pp. 2095–2128, Dec. 2012.
- [3] G. Tinkoff et al., "American association for the surgery of trauma organ injury scale I: Spleen, liver, and kidney, validation based on the national trauma data bank," *J. Amer. College Surgeons*, vol. 207, no. 5, pp. 646–655, Nov. 2008.
- [4] R. K. Latif et al., "Traumatic hemorrhage and chain of survival," *Scand. J. Trauma Resuscitation Emerg. Med.*, vol. 31, no. 1, May 2023, Art. no. 25.
- [5] A. Sauaia et al., "Epidemiology of trauma deaths: A reassessment," *J. Trauma Acute Care Surg.*, vol. 38, no. 2, pp. 185–193, Feb. 1995.
- [6] B. J. Eastridge et al., "Death on the battlefield (2001–2011): Implications for the future of combat casualty care," *J. Trauma Acute Care Surg.*, vol. 73, no. 6, pp. S431–S437, Dec. 2012.
- [7] J. S. Davis et al., "An analysis of prehospital deaths: Who can we save?," *J. Trauma Acute Care Surg.*, vol. 77, no. 2, pp. 213–218, Aug. 2014.
- [8] C. Schoeneberg, M. Schilling, B. Hussmann, D. Schmitz, S. Lendemans, and S. Ruchholtz, "Preventable and potentially preventable deaths in severely injured patients: A retrospective analysis including patterns of errors," *Eur. J. Trauma Emerg. Surg.*, vol. 43, no. 4, pp. 481–489, Aug. 2017.
- [9] E. R. Donley, S. Munakomi, and J. W. Loyd, *Hemorrhage Control*. Treasure Island, FL, USA: StatPearls Publishing, 2023.
- [10] B. J. Eastridge, J. B. Holcomb, and S. Shackelford, "Outcomes of traumatic hemorrhagic shock and the epidemiology of preventable death from injury," *Transfusion*, vol. 59, no. S2, pp. 1423–1428, 2019.
- [11] A. Stannard, J. J. Morrison, D. J. Scott, R. A. Ivatury, J. D. Ross, and T. E. Rasmussen, "The epidemiology of noncompressible torso hemorrhage in the wars in Iraq and Afghanistan," *J. Trauma Acute Care Surg.*, vol. 74, no. 3, pp. 830–834, Mar. 2013.
- [12] M. Di Serafino et al., "The technique and advantages of contrast-enhanced ultrasound in the diagnosis and follow-up of traumatic abdomen solid organ injuries," *Diagnostics*, vol. 12, no. 2, Feb. 2022, Art. no. 435.
- [13] J. R. Wortman, W. Landman, U. P. Fulwadha, S. G. Viscomi, and A. D. Sodickson, "CT angiography for acute gastrointestinal bleeding: What the radiologist needs to know," *Brit. J. Radiol.*, vol. 90, no. 1075, Jul. 2017, Art. no. 20170076.

- [14] T. M. Scalea et al., "focused assessment with sonography for trauma (FAST): Results from an international consensus conference," *J. Trauma Acute Care Surg.*, vol. 46, no. 3, pp. 466–472, Mar. 1999.
- [15] W. S. Do et al., "Too fast, or not fast enough? The FAST exam in patients with non-compressible torso hemorrhage," *Amer. J. Surg.*, vol. 217, no. 5, pp. 882–886, May 2019.
- [16] N. J. Carter and D. Gay, "FAST in the deployed military setting," *BMJ Mil. Health*, vol. 164, no. 5, pp. 332–334, Sep. 2018.
- [17] E. Sellon, S. Durdle, and D. Bailey, "Assessing the utility of ultrasound in the role 2 hospital setting," *BMJ Mil. Health*, vol. 167, no. 5, pp. 323–326, Oct. 2021.
- [18] M. Claudon et al., "Guidelines and good clinical practice recommendations for contrast enhanced ultrasound (CEUS) - update 2008," *Ultraschall der Medizin - Eur. J. Ultrasound*, vol. 29, no. 01, pp. 28–44, Feb. 2008.
- [19] V. Paefgen, D. Doleschel, and F. Kiessling, "Evolution of contrast agents for ultrasound imaging and ultrasound-mediated drug delivery," *Front. Pharmacol.*, vol. 6, Sep. 2015, Art. no. 197.
- [20] J. Jakobsen et al., "Safety of ultrasound contrast agents," *Eur. Radiol.*, vol. 15, no. 5, pp. 941–945, May 2005.
- [21] G. ter Haar, "Safety and bio-effects of ultrasound contrast agents," *Med. Biol. Eng. Comput.*, vol. 47, no. 8, pp. 893–900, Aug. 2009.
- [22] H. Yusefi and B. Helfield, "Ultrasound contrast imaging: Fundamentals and emerging technology," *Front. Phys.*, vol. 10, 2022, Art. no. 791145.
- [23] E. C. Unger, T. Porter, W. Culp, R. Labell, T. Matsunaga, and R. Zutshi, "Therapeutic applications of lipid-coated microbubbles," *Adv. Drug Del. Rev.*, vol. 56, no. 9, pp. 1291–1314, May 2004.
- [24] M. R. Rudnick, A. K. Leonberg-Yoo, H. I. Litt, R. M. Cohen, S. Hilton, and P. P. Reese, "The controversy of contrast-induced nephropathy with intravenous contrast: What is the risk?," *Amer. J. Kidney Dis.: Official J. Nat. Kidney Found.*, vol. 75, no. 1, pp. 105–113, Jan. 2020.
- [25] J. C. Weinreb et al., "Use of intravenous gadolinium-based contrast media in patients with kidney disease: Consensus statements from the american college of radiology and the national kidney foundation," *Radiology*, vol. 298, no. 1, pp. 28–35, Jan. 2021.
- [26] B. Sutarjono, M. Kessel, D. Alexander, and E. Grewal, "Is it time to re-think FAST? A systematic review and meta-analysis of Contrast-Enhanced Ultrasound (CEUS) and conventional ultrasound for initial assessment of abdominal trauma," *BMC Emerg. Med.*, vol. 23, no. 1, Jan. 2023, Art. no. 8.
- [27] B. S. Brenda and E. Tester, "Emerging applications of contrast-enhanced ultrasound in trauma," *Adv. Ultrasound Diagnosis Therapy*, vol. 6, no. 2, pp. 39–47, Jun. 2022.
- [28] A. J. Gale, "Current understanding of hemostasis," *Toxicologic Pathol.*, vol. 39, no. 1, pp. 273–280, Jan. 2011.
- [29] G. M. Currie, "Pharmacology Part 5: CT MRI Contrast Media," *J. Nucl. Med. Technol.*, vol. 47, no. 3, pp. 189–202, Sep. 2019.
- [30] K. Christensen-Jeffries et al., "Super-resolution ultrasound imaging," *Ultrasound Med. Biol.*, vol. 46, no. 4, pp. 865–891, Apr. 2020.
- [31] H.-m. Yi, M. R. Lowerison, P.-f. Song, and W. Zhang, "A review of clinical applications for super-resolution ultrasound localization microscopy," *Curr. Med. Sci.*, vol. 42, no. 1, pp. 1–16, Feb. 2022.
- [32] P. Song, J. M. Rubin, and M. R. Lowerison, "Super-resolution ultrasound microvascular imaging: Is it ready for clinical use?," *Zeitschrift für Medizinische Physik*, vol. 33, no. 3, pp. 309–323, Aug. 2023.
- [33] F. Pinto, M. Valentino, L. Romanini, R. Basilico, and V. Miele, "The role of CEUS in the assessment of haemodynamically stable patients with blunt abdominal trauma," *La Radiologia Medica*, vol. 120, no. 1, pp. 3–11, Jan. 2015.
- [34] C. L. Piccolo, M. Trinci, A. Pinto, L. Brunese, and V. Miele, "Role of contrast-enhanced ultrasound (CEUS) in the diagnosis and management of traumatic splenic injuries," *J. Ultrasound*, vol. 21, no. 4, pp. 315–327, Oct. 2018.
- [35] S. H. Roy-Choudhury et al., "Relative threshold of detection of active arterial bleeding: In vitro comparison of MDCT and digital subtraction angiography," *Amer. J. Roentgenol.*, vol. 189, no. 5, pp. W238–W246, Nov. 2007.
- [36] D. M. King, N. J. Hangiandreou, D. J. Tradup, and S. F. Stekel, "Evaluation of a low-cost liquid ultrasound test object for detection of transducer artefacts," *Phys. Med. Biol.*, vol. 55, no. 23, Nov. 2010, Art. no. N557.
- [37] C. Kargel, G. Hobenreich, B. Trummer, and M. Insana, "Adaptive clutter rejection filtering in ultrasonic strain-flow imaging," *IEEE Trans. Ultrasonics, Ferroelectr., Freq. Control*, vol. 50, no. 7, pp. 824–835, Jul. 2003.
- [38] C. Demené et al., "Spatiotemporal clutter filtering of ultrafast ultrasound data highly increases doppler and fUltrasound sensitivity," *IEEE Trans. Med. Imag.*, vol. 34, no. 11, pp. 2271–2285, Nov. 2015.
- [39] J. Baranger, B. Arnal, F. Perren, O. Baud, M. Tanter, and C. Demené, "Adaptive spatiotemporal SVD clutter filtering for ultrafast doppler imaging using similarity of spatial singular vectors," *IEEE Trans. Med. Imag.*, vol. 37, no. 7, pp. 1574–1586, Jul. 2018.
- [40] C. Huang et al., "Short acquisition time super-resolution ultrasound microvessel imaging via microbubble separation," *Sci. Rep.*, vol. 10, no. 1, Apr. 2020, Art. no. 6007.
- [41] R. J. Hanisch, R. L. White, and R. L. Gilliland, "Deconvolutions of hubble space telescope images and spectra," *Deconvolution of Images and Spectra*, P. A. Jansson, 2nd ed., Cambridge, MA, USA: Academic Press, 1997.
- [42] D. S. C. Biggs and M. Andrews, "Acceleration of iterative image restoration algorithms," *Appl. Opt.*, vol. 36, no. 8, pp. 1766–1775, Mar. 1997.
- [43] A. Rodriguez-Molares et al., "The generalized contrast-to-noise ratio: A formal definition for lesion detectability," *IEEE Trans. Ultrasonics, Ferroelectr., Freq. Control*, vol. 67, no. 4, pp. 745–759, Apr. 2020.
- [44] B. L. Welch, "The generalization of students problem when several different population variances are involved," *Biometrika*, vol. 34, no. 1/2, pp. 28–35, Jan. 1947.
- [45] S. Schoen Jr, Z. Zhao, A. Alva, C. Huang, S. Chen, and C. Arvanitis, "Morphological reconstruction improves microvessel mapping in super-resolution ultrasound," *IEEE Trans. Ultrason., Ferroelectr., Freq. Control*, vol. 68, no. 6, pp. 2141–2149, Jun. 2021.
- [46] S. Schoen, A. E. Samir, and V. Kumar, "MR for ULTRA-SR: Improved localization with morphological image processing," in *Proc. IEEE Int. Ultrason. Symp.*, 2022, pp. 1–4.
- [47] M. A. Averkiou, M. F. Bruce, J. E. Powers, P. S. Sheeran, and P. N. Burns, "Imaging methods for ultrasound contrast agents," *Ultrasound Med. Biol.*, vol. 46, no. 3, pp. 498–517, Mar. 2020.
- [48] K. G. Brown and K. Hoyt, "Evaluation of nonlinear contrast pulse sequencing for use in super-resolution ultrasound imaging," *IEEE Trans. Ultrasonics, Ferroelectr., Freq. Control*, vol. 68, no. 11, pp. 3347–3361, Nov. 2021.
- [49] L. J. Brattain, B. A. Telfer, M. Dhyani, J. R. Grajo, and A. E. Samir, "Machine learning for medical ultrasound: Status, methods, and future opportunities," *Abdominal Radiol.*, vol. 43, no. 4, pp. 786–799, Apr. 2018.
- [50] R. J. G. van Sloun, O. Solomon, M. Bruce, Z. Z. Khaing, Y. C. Eldar, and M. Misch, "Deep learning for super-resolution vascular ultrasound imaging," in *Proc. IEEE Int. Conf. Acoust. Speech Signal Process.*, 2019, pp. 1055–1059.
- [51] R. J. G. van Sloun et al., "Super-resolution ultrasound localization microscopy through deep learning," *IEEE Trans. Med. Imag.*, vol. 40, no. 3, pp. 829–839, Mar. 2021.